

# The early optical afterglow and non-thermal components of GRB 060218

S. W. K. Emery<sup>1b</sup>,<sup>1★</sup> M. J. Page<sup>1b</sup>,<sup>1</sup> A. A. Breeveld,<sup>1</sup> P. J. Brown,<sup>2</sup> N. P. M. Kuin,<sup>1</sup>  
S. R. Oates<sup>3</sup> and M. De Pasquale<sup>4</sup>

<sup>1</sup>Mullard Space Science Laboratory, University College London, Holmbury St Mary, Dorking, Surrey RH5 6NT, UK

<sup>2</sup>George P. and Cynthia Woods Mitchell Institute for Fundamental Physics and Astronomy, Department of Physics and Astronomy, Texas A&M University, 4242 TAMU, College Station, TX 77843, USA

<sup>3</sup>Department of Physics, University of Warwick, Coventry CV4 7AL, UK

<sup>4</sup>İstanbul University Department of Astronomy and Space Sciences, 34119 Beyazıt, İstanbul, Turkey

Accepted 2019 February 5. Received 2018 November 13; in original form 2018 March 21

## ABSTRACT

We re-examine the UV/optical and X-ray observations of GRB 060218 during the prompt and afterglow phases. We present evidence in the UV/optical spectra that there is a synchrotron component contributing to the observed flux in the initial 1350 s. This result suggests that GRB 060218 is produced from a low-luminosity jet, which penetrates through its progenitor envelope after core collapse. The jet interacts with the surrounding medium to generate the UV/optical external shock synchrotron emission. After 1350 s, the thermal radiation in the UV/optical and X-ray becomes the dominant contribution to the observed flux. The UV/optical and X-ray spectra at 1350–10 000 s can be fitted with a spherically outflowing blackbody model, with an additional power-law component to the model at X-ray energies.

**Key words:** radiation mechanisms: non-thermal – radiation mechanisms: thermal – gamma-ray burst: general – gamma-ray burst: individual: GRB 060218.

## 1 INTRODUCTION

It has been known that there is an association between long gamma-ray bursts (GRBs) and supernovae (SNe) since the simultaneous discovery of GRB 980425 and SN 1998bw. This connection strengthened the notion that long-duration GRBs were caused by the core collapse of massive stars (Woosley, Heger & Weaver 2002). In the preferred model for long GRBs, the collapsar model, the core collapse of a massive star into a black hole or a neutron star with an accretion disc drives a highly relativistic jet, which penetrates the outer stellar envelope, producing a GRB (Woosley 1993). The relativistic jet begins to decelerate when it interacts with the external medium; this leads to the external shock afterglow, which radiates a significant fraction of the initial total energy (Mészáros & Rees 1997). A number of SNe have been identified spectroscopically following a number of GRBs; see Cano et al. (2017) for a recent list.

Some GRBs are observed at much lower luminosities ( $10^{46}$ – $10^{48}$  erg s<sup>−1</sup>) than typical GRBs ( $10^{50}$ – $10^{52}$  erg s<sup>−1</sup>); these bursts are classified as low-luminosity GRBs (LLGRBs). So far, six LLGRBs have been identified, four of which have corresponding spectroscopically confirmed SNe: GRB 980425 (SN 1998bw), GRB 031203 (SN 2003lw), GRB 060218 (SN 2006aj), and GRB 100316D (SN 2010bh). GRB 111005A was identified as an LLGRB

with a redshift of  $z = 0.0133$ ; however, an associated SN was not found (Michałowski et al. 2018). GRB 170817A was a short GRB that produced gravitational waves, GW 170817, detected by LIGO, and was associated with a blue kilonova at a redshift of  $z = 0.009$  (Abbott et al. 2017). Within this sample of four LLGRBs associated with SNe, two have regular long GRB durations ( $\sim 20$  s), and two have ultralong durations ( $\sim 2000$  s); all four have smooth gamma-ray light curves. Soderberg et al. (2006) estimated the volumetric rate to be a factor of 100 times greater than that of typical long GRBs. All detected LLGRBs occurred nearby ( $\sim 40$ – $400$  Mpc); it is a consequence of their luminosities being low, which implies that unless they occur close to us, they do not trigger current detectors.

One such LLGRB and associated SN are GRB 060218 (Campana et al. 2006) and SN 2006aj (Cusumano et al. 2006), respectively. GRB 060218, like other LLGRBs, is shown to be faint and soft with a smooth gamma-ray light curve. However, we can study GRB 060218 in great detail, due to the extensive coverage of the observations in the UV/optical bands, days before the Ni<sup>56</sup>-decay-powered emission from SN 2006aj was observed. This coverage allows us to examine the emission before the optical SN emission, and enables us to investigate the link between the outflow components of both GRB 060218 and SN 2006aj.

GRB 060218 was first detected by the Burst Alert Telescope (BAT; Barthelmy et al. 2005) onboard *The Neil Gehrels Swift Observatory* (Gehrels et al. 2004). A very long  $T_{90}$  (the duration containing 90 per cent of the gamma-ray flux) (Kouveliotou et al. 1993) was measured from the BAT gamma-ray light curve of

\* E-mail: ucasswk@ucl.ac.uk

2100  $\pm$  100 s and GRB 060218 is therefore considered to be an ultralong GRB ( $T_{90} > 1000$  s) (Virgili et al. 2013). GRB 060218 had a redshift of  $z = 0.0331$  (Sollerman et al. 2006), making it the fourth nearest GRB with a determined redshift, after GRB 111005A (Michałowski et al. 2018), GRB 170817A (Abbott et al. 2017), and GRB 980425 (Galama et al. 1998). The gamma-ray spectrum of GRB 060218 is atypically soft for a long GRB, with an average peak energy  $E_{\text{peak}} = 4.9^{+0.4}_{-0.3}$  keV (Campana et al. 2006). The isotropic equivalent emitted energy was calculated as  $E_{\text{iso}} = (6.2 \pm 0.3) \times 10^{49}$  erg, extrapolated to the 1–10 000 keV rest-frame energy band (Campana et al. 2006).

While GRB 060218 exhibits a low  $E_{\text{peak}}$  and an  $E_{\text{iso}}$  that is four orders of magnitude smaller than the value for typical long GRBs (Sazonov, Lutovinov & Sunyaev 2004; Campana et al. 2006), GRB 060218 adheres to the Amati correlation (Campana et al. 2006), linking  $E_{\text{peak}}$  and  $E_{\text{iso}}$  (Amati et al. 2002). Furthermore, Liang et al. (2006) showed that GRB 060218 conforms to the luminosity–lag relation, a relationship seen in many long GRBs (Norris, Marani & Bonnell 2000; Ukwatta et al. 2012). This is a correlation between the GRB isotropic peak luminosity and spectral lag, where the lag is defined as the difference in time of arrivals of high- and low-energy photons. The luminosity–lag relation observed in GRB 060218, coupled with its compliance with the Amati correlation, indicates that GRB 060218 has similar radiation physics to long GRBs (Liang et al. 2006), despite being a low-luminosity, ultralong GRB. However, it has been argued that the prompt X-ray emission in GRB 060218 is produced by shock breakout emission (Waxman, Mészáros & Campana 2007; Nakar 2015). Furthermore, Nakar (2015) suggested that all high-energy emission of LLGRBs is entirely due to shock breakout emission (Nakar 2015).

The Ultraviolet Optical Telescope (UVOT; Roming et al. 2005) onboard *Swift* observed strong UV/optical emission, both during the prompt gamma-ray emission and for days following the trigger, with good coverage. *Swift* also provided simultaneous observations from the X-ray Telescope (XRT; Burrows et al. 2005). The observed X-ray flux rose to a peak luminosity of  $\sim 3 \times 10^{46}$  erg s $^{-1}$  (0.3–10 keV). The peak in the X-ray flux was followed by a fast decay, and at  $\sim 10^4$  s the flux began to decrease at a steady rate as a power law ( $F_{\nu} \propto t^{-1.1}$ ); this decreasing phase lasted for several days. During the initial 10 ks, there is a thermal blackbody component in the X-ray spectra, which ranges in  $kT$  from 0.05 to 0.12 keV. The UV/optical light curve shows a continuously rising UV and optical profile until it peaks in luminosity at  $\sim 30$  ks, after which the source fades, and then the Ni $^{56}$ -decay-powered emission from SN 2006aj is observed rising in the  $V$  band at  $\sim 200$  ks. During the initial 3000 s, GRB 060218 was observed with good time coverage in the UV/optical bands with UVOT. The coverage enables the UV/optical spectra to be examined systematically, and the search for a UV/optical afterglow can be performed with an in-depth analysis of the early UV/optical emission, something that is lacking in previous studies of GRB 060218. Due to the detection of both GRB 060218 and SN 2006aj, and the presence of a thermal component in the UV/optical and X-ray emission, a variety of models have been put forward to explain the observations. Campana et al. (2006) and Waxman et al. (2007) modelled the thermal emission as being produced from the breakout of a shock driven by a mildly relativistic shell, where the radiation generated by the shock travels through a dense wind surrounding the Wolf–Rayet (WR) progenitor star of the SN.

In this model, the shock reaches a region where the optical depth of the stellar envelope is low enough that the photons from the shock

escape, producing a bright flash in the UV and X-ray (Waxman et al. 2007). Waxman et al. (2007) suggested that this takes place at a breakout radius,  $R = 7.8 \times 10^{12}$  cm. Assuming spherical symmetry, the time it takes for the photons to escape the shock (the breakout duration) is the breakout radius divided by the speed of light. For a breakout radius of  $R = 7.8 \times 10^{12}$  cm, this corresponds to a duration of 260 s (Waxman et al. 2007). This duration is a lot shorter than the time it takes for the X-ray to peak in luminosity at 1000 s. Waxman et al. (2007) argued that an anisotropic shock will change the time-scale, as the time-scale would not be represented by  $R/c$ , but rather a time-scale influenced by an angular velocity profile in an anisotropic shell (Waxman et al. 2007). Waxman et al. (2007) suggested that an optically thick wind would increase the breakout radius and therefore argued that the shock breakout occurred in the wind around the envelope. Ghisellini, Ghirlanda & Tavecchio (2007a) argued that fine tuning is required to achieve a longer breakout duration. Li (2007) presented a model that computed the characteristic quantities for the transient emission from the shock breakout in a Type Ibc SN, which follows the core collapse of a WR star in a dense wind region. When the model described by Li (2007) is applied to GRB 060218, the energy predicted for the shock breakout in the underlying SN is much lower than the measured energy of the thermal components, which was  $\gtrsim 10^{49}$  erg.

In keeping with the shock breakout model, Campana et al. (2006) and Waxman et al. (2007) suggested that the early UV/optical emission ( $t < 10$  ks) could be produced from the Rayleigh–Jeans tail of the thermal X-ray emission produced by a shock propagated into the wind surrounding the envelope. The UV/optical light curve would then be governed by the expansion of the wind and the decreasing temperature. Within this model, the emission in UV/optical at 120 ks is produced from the envelope of the star, which is initially hidden by the wind (Campana et al. 2006).

Ghisellini et al. (2007a) and Ghisellini, Ghirlanda & Tavecchio (2007b) propose that if the UV/optical radiation is a result of the Rayleigh–Jeans section of the blackbody spectrum, the implied blackbody luminosities are too high, particularly in the early times ( $t < 3000$  s). Therefore, Ghisellini et al. (2007a) argued that the emission mechanism that governs the observed UV/optical radiation is unclear at early times. Furthermore, Ghisellini et al. (2007a) argued that the spectrum across the UV/optical and X-ray can be produced from self-absorbed synchrotron emission, where the flux  $F \propto \nu^{2.5}$ . But they find that the model does not account for the thermal component in the X-rays. Therefore, Ghisellini et al. (2007a) proposed an alternative explanation for the origin of the thermal emission, in which the emission is produced at the transparency radius of a GRB jet. Such an optically thick component from the jet photosphere has been observed in the prompt gamma-ray emission from GRB 100724B (Guiriec et al. 2011) and also GRB 110205A (Guiriec et al. 2016). However, this component is distinctly different to the shock-heated expanding envelope proposed by Waxman et al. (2007), which they argue describes the thermal component in the UV/optical emission at 120 ks.

By investigating the radio observations of GRB 060218, Soderberg et al. (2006) conclude that the radio emission is dominated by synchrotron self-absorbed emission, and the emission is from a mildly relativistic outflow ( $\Gamma = 2.3$ ). Soderberg et al. (2006) also show that due to the lack of jet break in the radio up until 22 d, the opening angle of the outflow can be constrained to  $\theta_0 > 1.4$  rad. Furthermore, based on the same observations, Soderberg et al. (2006) rule out an off-axis jet, where the angle from the line of sight to the jet axis is double the opening angle,  $\theta_{\text{obs}} = 2\theta_j$ .

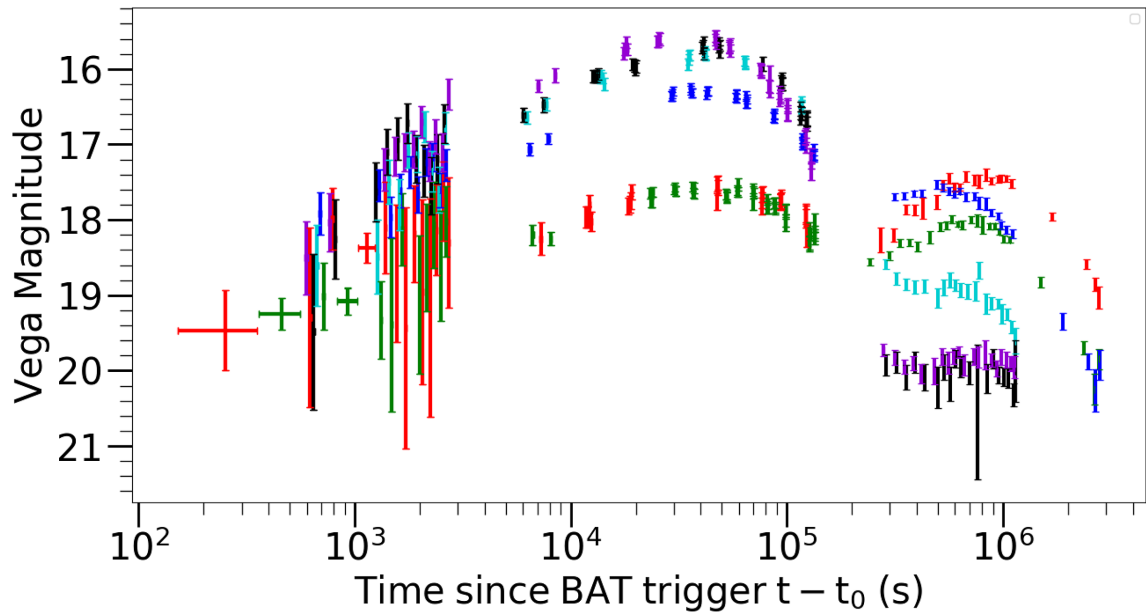


**Figure 1.** The UV/optical light curves of GRB 060218 in six UVOT filters. The colours represent the different UVOT filters: *V* as red points, *B* as green, *U* as blue, *UVW1* as turquoise, *UVM2* as black, and *UVW2* as violet. The light curve is not binned before 150 ks and has been binned at late times ( $>150$  ks) to increase the signal-to-noise ratio ( $S/N > 2$ ).

Toma et al. (2007) argued that the radio afterglow was produced by a non-relativistic phase of an initially collimated jet within the external shock synchrotron model, and showed that it is possible for a jet, with an opening angle  $\theta_0 \simeq 0.3$  rad and an initial Lorentz factor  $\Gamma_0 \simeq 5$ , to penetrate the stellar envelope.

In this paper, we present a detailed breakdown of the observations of GRB 060218, with a particular focus on the UV/optical and X-ray emission. Our goal is to determine what the mechanisms are that produce the emission from GRB 060218 and SN 2006aj. We pay particular attention to the early spectral evolution in the UV/optical emission, and study the thermal component across the optical to X-ray energy range. In Section 2 we provide a summary of the data reduction methods and describe the models and fitting techniques. The results of our analysis are given in Section 3. The implications of this analysis are discussed in Section 4.

We will use the convention for power laws:  $F_\nu \propto t^{-\alpha} \nu^{-\beta}$ , where  $F_\nu$  is the flux density,  $t$  and  $\nu$  are time and frequency,  $\alpha$  and  $\beta$  are the temporal and spectral indices, respectively (Sari, Piran & Narayan 1998). We use a subscript to denote the waveband of interest, so the spectral index for X-ray spectra is  $\beta_X$  and that for UV/optical spectra is  $\beta_{UV}$ . Throughout this paper, we use the values measured in Planck Collaboration I (2016) for the Hubble parameter  $H_0 = 67.8 \text{ km s}^{-1} \text{ Mpc}^{-1}$  and density parameters  $\Omega_\Lambda = 0.69$  and  $\Omega_m = 0.31$ . Uncertainties are quoted at  $1\sigma$  unless otherwise stated.

## 2 DATA REDUCTION AND ANALYSIS

### 2.1 Observations

GRB 060218 was detected with the BAT onboard *Swift* and *Swift* slewed autonomously to the burst. GRB 060218 was simultaneously observed with the XRT and UVOT after the trigger, and observations continued until both GRB 060218 and SN 2006aj were no longer detectable. Due to the rising UV/optical flux in the initial 60 ks and the identification of SN 2006aj at 10 d past the trigger, GRB

060218 and SN 2006aj were observed with excellent coverage in both UVOT and XRT.

### 2.2 UVOT data

We started with the sky images that had been produced by the pipeline processing. These images are mod-8 corrected, and aspect corrected to ensure the correct sky coordinates.

Count rates were obtained using the standard UVOT FTOOLS: UVOTMAGHIST software from HEASOFT (version 6.7). When the source was brighter than 1 count per second, the standard aperture for UVOT photometry of radius 5 arcsec was implemented. When the source was fainter than 1 count per second a source aperture of radius 3 arcsec was selected to maintain a good signal-to-noise ratio and aperture corrected to 5 arcsec (Poole et al. 2008; Breeveld et al. 2010). Background was measured from a large region offset from the source position. The background area was chosen to be free of any contaminating sources, and large enough that weak contaminating sources did not contribute to the mean count rate significantly. Magnitudes were calculated using the observed count rates and the UVOT zero-points from Breeveld et al. (2011). The count rates were not host galaxy subtracted, because the host galaxy was not detected in any UVOT bands in our source aperture.

Fig. 1 shows the UV/optical light curves. At 138 s after the trigger time, the UVOT started taking data. The *V* and *B* finding charts were taken with 200 s long exposures each after the 9 s settling exposure in the *V* filter. We do not include the settling exposure in our analysis, because its duration is too short to be of much value.

In the initial 50 ks, we have created eight spectral energy distributions (SEDs) covering the UVOT energies. The time intervals for the SEDs are given in Table 1. The first SED was created after the finding charts were taken, at which point a 20 s image was taken in each filter. After the initial 1000 s, 20 s exposure images were taken in each filter every 200 s until  $\sim 3000$  s; therefore, five SEDs can be obtained during this time. After 3000 s the exposure time for each filter increased to 200 s. There were no observations between

**Table 1.** Times used for creating the UV/optical–X-ray SEDs. The SED central time is the central time from both the UV/optical and X-ray SED time ranges.

SED central time (s)	UVOT SED range (s)	X-ray SED range (s)
650	550–750	550–750
1250	1150–1350	1150–1350
1625	1400–1850	1400–1850
2125	1900–2350	1900–2350
2550	2400–2700	2400–2700
6500	6410–6590	6000–7000
7500	7410–7590	7000–8000
120 000	117 500–122 500	10 000–130 000

2700 and 5950 s due to GRB 060218 being occulted by the Earth during these times. Two SEDs can be obtained between 6000 and 8000 s, as GRB 060218 was observed in each filter twice during this interval.

When creating the SEDs, even though the exposures were taken close together in time, the magnitudes in different filters must be adjusted to common epochs. Therefore, a model of the light curve is required to determine the adjustments. For this purpose, a second-order polynomial curve was fitted to the UV/optical light curve (as magnitude against log time) in the interval 5–60 ks. Adjustments made before 5 ks were performed assuming a power law with a temporal index of  $\alpha = -0.7$ . For the adjustments made after 60 ks, we used a power-law decay with slopes determined individually for each filter.

### 2.3 XRT data

For the X-ray contribution to the SED, the X-ray event data were first cleaned using FTOOLS: XRTPIPELINE. Event data were selected in grades 0–12 for Photon Counting (PC) mode data and grades 0–2 for Windowed Timing (WT) mode data (Capaldi et al. 2005). The auxiliary response files were produced by FTOOLS: XRTMKARF. These response files contain the product of telescope area, filter efficiency, and quantum efficiency as a function of energy. The X-ray spectra were extracted using XSELECT (version 2.4c) and the energy range used to analyse the X-ray data was 0.3–10 keV.

The WT mode spectra were extracted from the event data with a circular region of radius 11 arcsec around the 1D image strip (rotated by the instrument roll angle). The background was removed using the same size region, shifted away from the source along the image strip. The PC mode spectra were extracted in the same way but from a 2D image. XRT spectra were grouped to a minimum of 20 counts in each bin, which allows the use of  $\chi^2$  statistics.

Where possible, the X-ray spectra were extracted over the same time intervals as the UV/optical spectra were taken. However, after 6000 s, larger durations were required to achieve adequate quality for the X-ray spectra. For all SEDs, the mid-points of the X-ray exposures were chosen to be equal to the mid-points of the corresponding UVOT time intervals, and the X-ray spectra were scaled to the corresponding count rate at the mid-point time. The time intervals used for the SEDs are shown in Table 1.

### 2.4 Analysis and modelling

The SEDs were analysed using XSPEC (version 12.9.0) and were modelled with a combination of power law and spherically outflowing blackbody components, together with photoelectric absorption

and dust extinction from our Galaxy and the host galaxy of the GRB. The Galactic reddening was fixed at  $E(B - V) = 0.14$ , based on the extinction maps in Schlegel, Finkbeiner & Davis (1998). The determination of the host-galaxy reddening is discussed in detail in Section 3. The X-ray absorption in our Galaxy is accounted for by fixing the hydrogen column density,  $N_H$ , in our galaxy for GRB 060218 to  $N_H = 1.0 \times 10^{21} \text{ cm}^{-2}$  (Kalberla et al. 2005); the host-galaxy absorption is a free parameter in the SED fitting.

#### 2.4.1 Spherically outflowing blackbody components

The blackbody emission from GRB 060218 is thought to arise in material flowing out from the stellar explosion at tens of thousands of  $\text{km s}^{-1}$  (Campana et al. 2006). To model the blackbody emission, we assume a spherically symmetric blackbody model.

However, the outflow of the blackbody component has not been included in the model fitted to the data for GRB 060218 before this study. To correctly describe the relativistic blackbody emission from a spherical outflow, relativistic beaming and Doppler shift must be taken into consideration. Due to relativistic effects, we observe the apparent flux, which is related to that in the blackbody rest frame through the Lorentz factor,  $\Gamma$ , the Doppler factor,  $\delta$ , and the angle of the outflow with respect to the line of sight from the observer,  $\theta$ . The Lorentz factor,  $\Gamma$ , is related to the intrinsic velocity of the outflow,  $v$ , by

$$\Gamma = (1 - (v/c)^2)^{-1/2}, \quad (1)$$

and the Doppler factor,  $\delta$ , is defined as

$$\delta = \Gamma^{-1}(1 - \frac{v}{c}\cos\theta)^{-1}. \quad (2)$$

The observed blackbody temperature,  $T$ , in relation to the temperature in the outflow frame,  $T_o$ , is given by

$$T = \delta T_o, \quad (3)$$

and the observed blackbody flux from a surface element,  $F_v$ , is given by

$$F_v = \frac{2\pi h v^3 \delta^3}{c^2} \frac{1}{e^{\frac{h\nu}{k\delta T_o}} - 1} \frac{A}{D^2}, \quad (4)$$

where  $A$  is the projected area of the emitter, and  $D$  is the distance between the emitter and the observer.

Our spherical outflowing blackbody model is composed by splitting the emitting surface into ten components according to the angle,  $\theta$ , with a corresponding line-of-sight velocity,  $v = v_0 \cos\theta$ , where  $v_0$  is the outflow velocity. In the simple single blackbody model, the outflow is observed with a projected area of  $A = \pi R^2$ , with radius  $R$ . In the spherical outflow model, this area is divided into ten ring components.

## 3 RESULTS

Using the observations of GRB 060218 and SN 2006aj taken in the first few days, we can use the colour ( $UVM2 - U$ ) and the X-ray light curve to help separate the observations into five different phases of evolution. Splitting the light curve into phases is useful because the spectral shape across the UV/optical and X-ray energy range changes substantially from the time of the GRB trigger until the  $\text{Ni}^{56}$ -decay-powered emission becomes the dominant source of emission in the optical energy range. The colour ( $UVM2 - U$ ) is used because it provides a good indication of the balance of UV versus optical radiation, which changes considerably over the course of the observations.



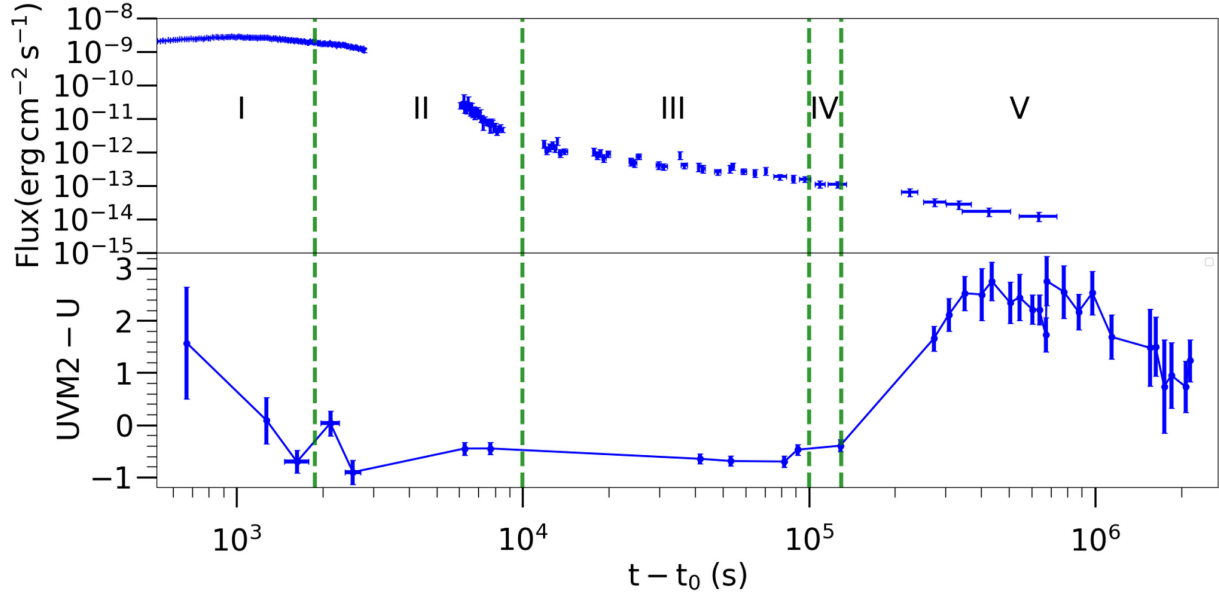


**Figure 2.** The figure shows in the top panel the X-ray light curve of GRB 060218 and in the bottom panel, the colour  $UVM2 - U$  of GRB 060218 from 650 s to 2000 ks. The plot is separated by four times to form five phases.

**Table 2.** Summary of emission components used to model the SEDs in each phase. In phase III, the temperature and radius of the outflowing blackbody cannot be determined because it peaks between the UV/optical and X-ray energies. Therefore, we have used simply a power law of  $\beta_{UV} = -2$  to represent the Rayleigh-Jeans tail in the UV/optical. In phase IV, the outflowing blackbody has no contribution in the X-ray spectra. No fits were done in phase V.

Phase	Time (s)	Emission components
I	159–1350	power law (UV/optical only) power law (X-ray only) outflowing blackbody
II	1350–10000	power law (X-ray only) outflowing blackbody
III	10000–100000	power law (X-ray only) Rayleigh-Jeans tail (UV/optical only)
IV	100000–130000	power law (X-ray only) outflowing blackbody

The X-ray light curve and colour ( $UVM2 - U$ ) are shown in Fig. 2. Phase I represents the period between the start of the UVOT and XRT observations at 159 s and the time when the UV/optical power-law component is no longer detected at 1350 s. The spectral change that characterizes Phase I is also clear in the spectral index calculations,  $\beta_{UV}$ , shown in Table 4 and Fig. 5. Phase II is the time when the colour ( $UVM2 - U$ ) is consistent with a constant value ( $UVM2 - U \sim -0.5$ ) and the thermal blackbody emission is visible at UV/optical and X-ray energies. The constant ( $UVM2 - U$ ) colour is expected when the UV/optical emission is dominated by the Rayleigh-Jeans tail of a blackbody.

The line at 10 ks, shown in Fig. 2, marks the end of the X-ray blackbody emission, and so the end of this phase. During phase III the X-ray emission has a power-law spectrum without any observed contribution from a thermal component. During phase IV the ( $UVM2 - U$ ) colour changes as the blackbody cools sufficiently

to peak in the UV. During Phase V the  $\text{Ni}^{56}$ -decay-powered emission from SN 2006aj becomes dominant at optical wavebands leading to a much redder colour in ( $UVM2 - U$ ). The red colour is because of line blanketing from iron-peak elements in the UV spectra, as seen for example in the *HST* UV spectra of SN 1994I in Millard et al. (1999).

Table 2 summarizes the components we used to model the SEDs for each phase.

### 3.1 Determination of the host-galaxy reddening

Before we examine the evolution of the SED, it is useful to determine the optical reddening due to dust in the host galaxy of the GRB. Previous works have argued that the UV/optical emission for times  $< 50$  ks is dominated by the Rayleigh-Jeans tail of the blackbody-like emission component (Campana et al. 2006; Waxman et al. 2007; Ghisellini et al. 2007a). During this period, we can determine the reddening rather precisely because the underlying spectrum has a well-understood spectral shape: a power law with spectral index,  $\beta_{UV} = -2$ .

In the interval 5–60 ks, we fitted second-order polynomials simultaneously to the light curves in the different UVOT filters. The polynomials were constrained to have the same shape (first- and second-order coefficient) but different offsets in the different bands, which allowed us to get the differences in magnitudes for each filter precisely while the colour was constant. The best-fitting set of parabolas is shown in Fig. 3. We created an SED at 40 ks, using the fitted magnitudes from our simultaneous fitting.

When modelling the SED, we can determine the best extinction curve  $k(\lambda)$ , and reddening values  $E(B - V)R_v$  from fitting, by fixing the known spectral index at  $\beta_{UV} = -2$ , because we assume that the UV/optical spectra have a Rayleigh-Jeans shape. We found that the Small Magellanic Cloud (SMC) and Large Magellanic Cloud (LMC) extinction curves produced acceptable fits with  $\chi^2/\text{dof} = 3.9/4$  and  $\chi^2/\text{dof} = 6.9/4$ , respectively. However, the Milky Way (MW) extinction curve can be excluded based on the  $\chi^2$ , where we found  $\chi^2/\text{dof} = 42.2/4$  corresponding to a null-hypothesis prob-

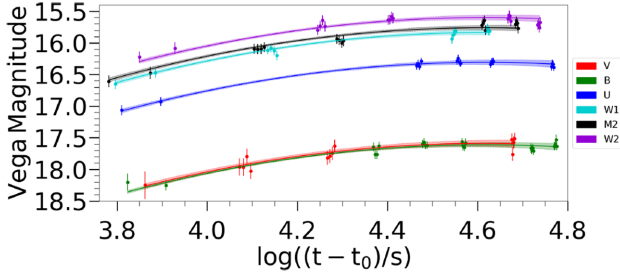


**Figure 3.** Light curves for GRB 060218 in the time range 5–60 ks. The six different colours represent the different UVOT filters. The best-fitting parabolic model light curves for each filter are shown as coloured lines, with associated  $1\sigma$  errors in the shaded regions.

**Table 3.** Host-galaxy extinction curve comparison.  $R_V$  is the extinction  $A_V$  divided by the colour excess  $E(B - V)$ .  $\chi^2/\text{dof}$  is the best-fitting chi-square/degrees of freedom and  $p$  is the corresponding null-hypothesis probability.

Extinction curve shape	$R_V$	$E(B - V)$ (mag)	$\chi^2/\nu$	$p$
SMC	2.93	$0.179 \pm 0.007$	3.9/4	0.41
LMC	3.16	$0.197 \pm 0.008$	6.9/4	0.14
MW	3.08	$0.215 \pm 0.009$	42.2/4	$1.6 \times 10^{-8}$

**Table 4.** Summary of the UVOT time-resolved SED fits for GRB 060218. Here we show the best-fitting chi-square,  $\chi^2$ , when comparing the fit of the spectral index,  $\beta_{UV}$  (4 dof), to the fixed Rayleigh–Jeans spectral shape,  $\beta_{UV} = -2$  (5 dof).  $p$  is the corresponding null-hypothesis probability.

Time (s)	$\beta_{UV}$ fitted			$\beta_{UV}$ fixed at $-2$	
	$\beta_{UV}$	$\chi^2$	$p$	$\chi^2$	$p$
650	$0.2 \pm 0.6$	2.37	0.67	15.3	$9.3e-3$
1250	$-0.5 \pm 0.3$	11.60	0.02	25.7	$1.0e-4$
1625	$-1.8 \pm 0.3$	4.37	0.36	4.6	0.47
2125	$-1.4 \pm 0.3$	2.92	0.57	7.2	0.21
2550	$-1.8 \pm 0.3$	4.11	0.39	4.5	0.48
6500	$-2.0 \pm 0.1$	7.75	0.10	7.8	0.17
7500	$-2.0 \pm 0.1$	8.21	0.08	8.2	0.14

ability  $p = 1.6 \times 10^{-8}$ . The SMC extinction curve provided the best fit and for this curve we obtained  $E(B - V) = 0.179 \pm 0.007$  mag. The details of the fits for each extinction curve are given in Table 3. Based on the result that minimizes the  $\chi^2$ , we use an SMC extinction curve and  $E(B - V) = 0.179$  to fit the host-galaxy extinction for all of our SEDs.

### 3.2 The early-time UV/optical emission

The evolution of the ( $UVM2 - U$ ) colour, evident in Fig. 2, at early times, suggests that the spectral slope in the UV/optical changes during phase I. This spectral change is confirmed by fitting an absorbed power-law model across the UV/optical energies in our SEDs. The parameters of the fits are shown in Table 4 together with the  $\chi^2/\text{dof}$  values for the fits and the associated  $p$  values. All of the  $p$  values are above 0.01, and hence we consider all of the fits to be acceptable. Fig. 4 shows how the spectral shape changes between 650 and 1625 s across the UV/optical energy range. Superimposed on the SEDs in Fig. 4 are the best-fitting power-law models for each epoch, shown in red. Additionally, the model with a fixed Rayleigh–

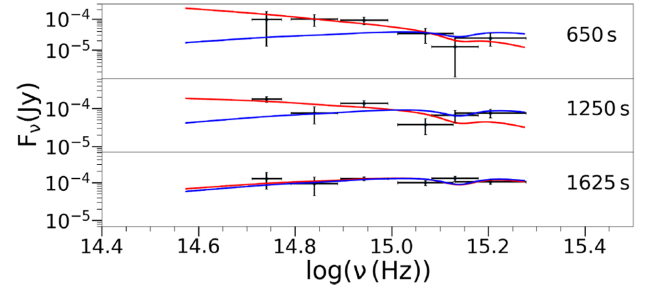


**Figure 4.** The SEDs of GRB 060218 at 650, 1250, and 1625 s. Each SED is fitted with a power-law model, with Galactic reddening  $E(B - V) = 0.14$  and host-galaxy reddening  $E(B - V) = 0.179$ . The red line represents the fitted power law whose results are shown in Table 2.2, and the blue line is the Rayleigh–Jeans power-law model with  $\beta_{UV}$  fixed at  $-2$ .

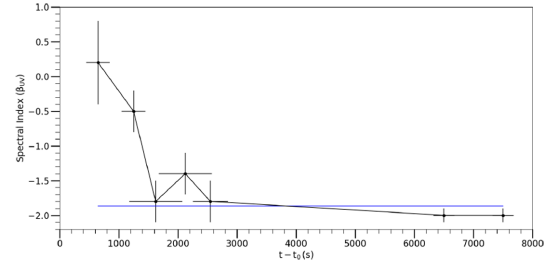


**Figure 5.** The best-fitting spectral indices,  $\beta_{UV}$ , to the UV/optical SEDs, from Table 4. The blue horizontal line shows an attempt to fit the values of  $\beta_{UV}$  with a constant (see Section 3.2).

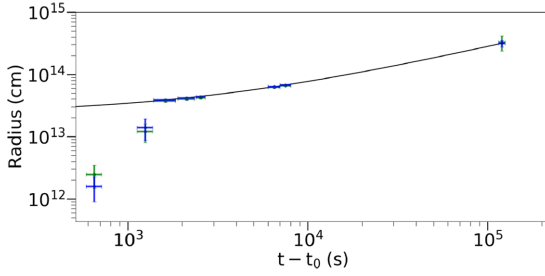
Jeans power-law index,  $\beta_{UV} = -2$ , is shown in blue. At 650 s the data are best modelled with fitted spectral index  $\beta_{UV} = 0.20^{+0.58}_{-0.63}$  and this value for the spectral index is consistent with the typical GRB afterglow spectral index,  $\langle \beta_{UV} \rangle = 0.66 \pm 0.04$ , (Kann et al. 2010; Schady et al. 2012). The UV/optical spectral shape evolves after 650 s and by 1625 s the UV/optical SED is consistent with a Rayleigh–Jeans slope.

Fig. 5 shows the fitted spectral index  $\beta_{UV}$  as a function of time. We have explicitly tested whether a single value of  $\beta_{UV}$  could fit all of the UV/optical SEDs by fitting a constant value to the power-law spectral indices (see Fig. 5). This fit results in a large chi-squared,  $\chi^2 = 38.7$  for 6 degrees of freedom with an associated null-hypothesis probability,  $p = 8.2e-7$ . Therefore, we can reject the hypothesis that the UV/optical emission can be characterized by a constant power-law spectral index.

We have also tested the consistency of each UV/optical SED with a Rayleigh–Jeans shape, which is equivalent to a power law with  $\beta_{UV}$  fixed at  $-2$ , by fitting such a model to each UV/optical SED. Table 4 includes  $\chi^2$  and associated null-hypothesis probabilities for these fits. This model does not fit well ( $p < 0.01$ ) for times  $< 1350$  s, but is an acceptable fit at later times. Therefore, a second component, in addition to the Rayleigh–Jeans emission, is needed to describe the UV/optical emission before 1350 s.

### 3.3 Fitting the full optical to X-ray SED

When analysing the X-ray and UV/optical emission, we fitted our SEDs with different models depending on the SED epoch. We took this approach because the UV/optical power-law component is not detected after phase I and also, the thermal emission component only contributes to the total X-ray radiation in the initial 10 ks. The



**Figure 6.** The radius against time, determined from fitting UV/optical/X-ray SEDs with a spherically outflowing blackbody component plus power-law model. The photospheric radii are shown with  $1\sigma$  errors in blue. The fitted photospheric radii using a stationary blackbody model are shown in green. The power-law plus constant model fit to the photospheric radii (equation 5) is shown as a black line.

combinations of components we used in our models for the different SED epochs are shown in Table 2.

For the phases that include the outflowing blackbody emission, we use a spherically outflowing blackbody model as described in Section 2.4.1. The blackbody model was initially fitted with the velocity of the outflow set to zero. However, the blackbody outflow velocity was not explicitly a free parameter in the model fits to the SEDs. The initial fitting of the blackbody model provides us with the blackbody emission radius against time. We calculate the velocity from the differential of a function that is fitted to the radius against time fit and iterate this new velocity until convergence of the parameters of the function. The fitted model and the model with zero velocity are shown in Fig. 6.

For all SED fits, the host-galaxy UV/optical reddening was fixed to the value discussed earlier,  $E(B - V) = 0.179$ . However, the host-galaxy X-ray absorption was left as a free parameter, because we have no prior knowledge of this.

When modelling the spherically outflowing blackbody model during phase I to our SEDs, we included a power-law component across the UV/optical energies, because there is a substantial power-law component during this time, as seen in Fig. 4. At 650 and 1250 s, we measured the flux of the power-law component in the UV/optical as  $\nu F_\nu(10^{15} \text{ Hz}) = (6 \pm 2)$  and  $(7 \pm 2) \times 10^{-13} \text{ erg cm}^{-2} \text{ s}^{-1}$ , contributing 99.5 and 82 per cent to the total flux, respectively.

Fitting our SEDs with our spherically outflowing blackbody model allows us to see the evolution of the blackbody (photospheric) radius over time. When modelling the radius, neither a linear model nor a power-law model provided acceptable fits to the

measurements, and so a power-law plus constant model was used; this model is represented by the black line in Fig. 6. The best-fitting parameters from our model are shown in equation (5),

$$R_{\text{BB}} = \left( (233 \pm 6) + (1.0 \pm 0.1)(t - t_0)^{0.68 \pm 0.01} \right) \times 10^{11} \text{ cm}, \quad (5)$$

where the radius can be expressed as  $R_{\text{BB}} = R_0 + A(t - t_0)^B$ , which gives the inferred blackbody radius in terms of the initial radius,  $R_0$ , and the time since the event was triggered,  $t - t_0$ . In this equation,  $A$  and  $B$  are free parameters determined in fitting. The value that we calculate,  $R_0 = (2.33 \pm 0.06) \times 10^{13} \text{ cm}$ , represents the radius at which the blackbody radiation is first released.

The power-law plus constant model was not fitted to the data at 650 and 1250 s because there is a large contribution to the X-ray flux from the prompt emission and a large contribution to the UV/optical flux from the afterglow component. As a consequence, we do not consider the constraints on the radius to be very reliable at these times. Furthermore, during the initial 800 s light traveltime affects the observed blackbody emission. At 650 s, we observe 85 per cent of the blackbody surface area emitted at an initial radius  $R_0 = (2.33 \pm 0.06) \times 10^{13} \text{ cm}$ . The effect would be more pronounced if the expansion is non-spherical. This could be the case in the early evolution of the outflow if a jet along the line of sight induces an aspherical outflow.

The results from the model fits to the SEDs are shown in Table 5. The measurements and model of the outflowing blackbody radius against time are displayed in Fig. 6. The full SEDs with the best-fitting models and the data/model ratios are given in Appendix A.

## 4 DISCUSSION

In this paper, we have given detailed analysis of the early UV/optical and X-ray emission from GRB 060218. There is a substantial change in the spectral shape of the early UV/optical emission, with the spectral index of the fitted power law changing by  $\Delta\beta_{\text{UV}} = 2.2 \pm 0.6$ . At 650 s after the GRB trigger, the spectral index across the UV/optical energies,  $\beta_{\text{UV}}$ , calculated from the SED power-law fit is  $\beta_{\text{UV}} = 0.20^{+0.58}_{-0.62}$ . The spectral index calculated from the UVOT SED power-law fit measured for different times shows an evolution in the spectral index, which quickly converges to a constant value of  $\beta_{\text{UV}}$ .

The UV/optical and X-ray emission can be characterized by a spherically outflowing blackbody plus power-law model for the times 1350–10 000 s. During this period, the power-law model is fitted only over the X-ray energy range in our SEDs.

**Table 5.** Summary of results for SED fits of GRB 060218 modelled with a spherical outflowing blackbody component.  $N_{\text{H}}$  represents the hydrogen column density, and  $kT$  and  $R$  are the energy and radius of the fitted blackbody component, respectively.  $\beta_X$  is the spectral index from the power-law component from the fitted model across the X-ray energy range, and  $\beta_{\text{UV}}$  is the spectral index from the power-law component from the fitted model across the UV/optical energy range.  $v/c$  is the converged value of the velocity/ $c$  for the spherically outflowing blackbody.  $\chi^2/\text{dof}$  is the best-fitting chi-square/degrees of freedom. For the SED at 120 ks, the fitted model included a blackbody component only at UV/optical energies.

Time (s)	$N_{\text{H}}$ ( $10^{-22} \text{ cm}^{-2}$ )	$kT$ (eV)	Blackbody radius $R$ ( $10^{13} \text{ cm}$ )	$\beta_X$	$\beta_{\text{UV}}$	$(v/c)$	$\chi^2/\text{dof}$
650	$0.58 \pm 0.04$	$117 \pm 14$	$0.16 \pm 0.07$	$0.42 \pm 0.03$	$0.21 \pm 0.63$	0.292	311.3/327
1250	$0.94 \pm 0.04$	$84.7 \pm 6.0$	$1.40 \pm 0.50$	$1.00 \pm 0.03$	$-0.17 \pm 0.43$	0.237	381.4/326
1625	$1.09 \pm 0.01$	$73.9 \pm 0.6$	$3.94 \pm 0.12$	$1.38 \pm 0.01$	—	0.218	637.4/529
2125	$1.08 \pm 0.01$	$74.4 \pm 0.3$	$4.20 \pm 0.13$	$1.67 \pm 0.02$	—	0.199	500.3/456
2550	$1.09 \pm 0.01$	$74.2 \pm 0.5$	$4.39 \pm 0.17$	$1.86 \pm 0.03$	—	0.189	431.9/323
6500	$1.28 \pm 0.02$	$56.2 \pm 0.8$	$6.34 \pm 0.01$	$2.61 \pm 0.19$	—	0.140	32.7/25
7500	$1.55 \pm 0.03$	$52.4 \pm 1.0$	$7.25 \pm 0.09$	$2.70 \pm 0.25$	—	0.134	19.2/17
120 000	$0.52 \pm 0.07$	$3.9 \pm 0.4$	$31.5 \pm 3.7$	$3.33 \pm 0.35$	—	0.056	42.6/26

In the initial 1350 s, the UV/optical power-law component has a higher contribution to the overall flux in the UV/optical than the blackbody component. For times after 1350 s, the thermal component in the UV/optical and X-ray spectra is the dominant source of the observed luminosity. After 10 ks, there is no longer an observed thermal component in the X-ray spectrum.

At 120 ks, the blackbody cools sufficiently to peak in the UV, and we measure the UV blackbody temperature. After 130 ks, the UV/optical flux is predominantly produced by the  $\text{Ni}^{56}$ -decay-powered emission, and the X-ray spectrum is still characterized by a soft power law.

#### 4.1 Origin of UV/optical emission before the SN peak

We measured the UV/optical spectral index at 650 s as  $\beta_{UV} = 0.20^{+0.58}_{-0.62}$ . Within  $1\sigma$ , this spectral index is consistent with the mean value of GRB afterglow spectral indices as calculated by Kann et al. (2010); Schady et al. (2012),  $\langle\beta_{UV}\rangle = 0.66 \pm 0.04$ . Similar to typical GRB afterglows, the emission mechanism that produces the spectral slope at 650 s is likely to be synchrotron emission. Typically, the synchrotron spectrum extends from the UV/optical to X-ray. However, this cannot be tested in GRB 060218 because the prompt emission still dominates the X-ray at early times (Toma et al. 2007). If the power-law model, which best fits the UV/optical data at 650 s, is extrapolated to the X-ray band, it represents only one fifth of the observed X-ray flux. Therefore, the early UV/optical spectra are consistent with the UV/optical emission being the afterglow, where the emission is produced by the interaction of a jet with the circumburst medium. At the date of writing, this is the first observation of a UV/optical afterglow in a low-luminosity GRB.

The observations at times 1350–60 000 s suggest that the UV/optical emission is dominated by emission from the Rayleigh-Jeans part of a blackbody spectrum. At 120 ks, the peak of the blackbody emission has moved into the UV/optical, with  $kT = 3.9 \pm 0.5$  eV at an inferred blackbody radius,  $R = (3.2 \pm 0.4) \times 10^{14}$  cm. The observations of the blackbody peaking in the UV/optical are in agreement with the expanding shock-heated wind model proposed in Waxman et al. (2007), Nakar (2015), and Irwin & Chevalier (2016). However, the expanding shock-heated wind model cannot explain the spectral shape before 1350 s. Therefore, we have two contributions to the total observed UV/optical flux: the synchrotron component, and the blackbody component; both components are observed simultaneously. It is for this reason that we argue that the non-thermal UV/optical emission is observed outside the optically thick expanding shock-heated wind. The characteristics of the non-thermal UV/optical emission are comparable to typical GRB afterglows; therefore, we propose that the non-thermal UV/optical emission is generated from the external shocks as the jet is slowed by the surrounding interstellar medium (ISM).

Ghisellini et al. (2007a) interpret the UV/optical emission for times <100 ks, as being produced through self-absorbed synchrotron emission. For this model, Ghisellini et al. (2007a) require the UV/optical spectrum to be  $\propto \nu^{2.5}$ . They can accommodate this value by using a value of the reddening,  $E(B - V) = 0.3$  mag, 0.12 greater than the value we derived from the techniques discussed in Section 3, where we argue that the UV/optical is on the Rayleigh-Jeans tail of the blackbody that is peaking in X-ray energies. However, the model used in Ghisellini et al. (2007a) only addresses the UV/optical emission during the initial 100 ks and does not account for the UV/optical spectral shape changing to resemble a blackbody that peaks in the UV/optical energy range at 120 ks. Additionally, the model used in Ghisellini et al. (2007a) does

not account naturally for the blackbody component in the X-ray emission, and they argue that this requires an additional component to explain the thermal X-ray emission. However, we have shown that the thermal X-ray emission can be emitted simultaneously from the same radius as the UV/optical blackbody emission. Therefore, our model addresses areas that Ghisellini et al. (2007a) did not, providing a more holistic explanation of the non-thermal and thermal components of the UV/optical emission.

#### 4.2 Existence of a jet?

As described in Section 4.1, the observations of the non-thermal UV/optical emission in the initial 1350 s suggest that the early UV/optical emission is synchrotron radiation. The synchrotron emission is likely due to the interaction of the GRB outflow with the circumburst region, which is predicted in the external shock model (Mészáros & Rees 1997). Furthermore, Toma et al. (2007) analysed the X-ray–Gamma-ray SED from BAT and XRT and showed that the non-thermal emission in the prompt phase of the GRB can be modelled well with a band function (Band et al. 1993). The low- and high-energy indices, from this model, are consistent with typical values of typical GRBs (Toma et al. 2007) where the emission is thought to be from a jet outflow. Therefore, both the prompt emission spectral characteristics and the presence of non-thermal emission in the UV/optical at early times point towards a scenario in which the jet has penetrated the optically thick envelope.

There are predominantly two models that attempt to reconcile the radio observations of GRB 060218. The first is put forward by Soderberg et al. (2006), who argue that the observed radio afterglow requires a mildly relativistic ( $\Gamma \gtrsim 2$ ) outflow interacting with the surrounding medium. Soderberg et al. (2006) and Fan, Piran & Xu (2006) suggest that this could be an effectively spherical, wide outflow with  $\theta_j \gtrsim 1$  rad, due to the lack of jet break in the radio observations up to 22 d. In order to model the radio light curves, Soderberg et al. (2006) require an isotropic kinetic energy,  $E_{k, \text{iso}} \sim 10^{48}$  erg, circumburst density,  $n \sim 10^2 \text{ cm}^{-3}$ , and the ratios of the electron and magnetic field energy density to the total thermal energy,  $\epsilon_e \sim 10^{-1}$  and  $\epsilon_B \sim 10^{-1}$ , respectively. However the gamma-ray efficiency is too high,  $\eta_\gamma = \frac{E_{\text{iso}, \gamma}}{E_{\text{iso}, \gamma} + E_{k, \text{iso}}} \approx 98$  per cent.

An alternative model that helps resolve the gamma-ray efficiency problem was offered by Toma et al. (2007), where the radio emission is produced by the external shock synchrotron model, which requires a jet with an initial Lorentz factor,  $\Gamma_0 = 5$ , where  $\Gamma_0$  is the initial Lorentz factor of the jet just as it exits the star (Toma et al. 2007). In this model, the radio emission is produced in the non-relativistic phase of the outflow and requires an opening angle of  $\theta_0 = 0.3$  rad (Toma et al. 2007), which is smaller than the opening angle required in the models proposed by Soderberg et al. (2006) and Fan et al. (2006). The opening angle was required by Toma et al. (2007) to obtain a reasonable gamma-ray efficiency and also to satisfy a condition that was needed for the jet to penetrate the stellar envelope. Toma et al. (2007) remark that the jet could initially be collimated, to penetrate the progenitor envelope, like in the standard collapsar model (Woosley 1993; MacFadyen & Woosley 1999). They explain that the radio emission is observed at a period where the initially collimated jet moves towards a spherical geometry.

At 650 and 1250 s, the UV/optical fluxes of the power-law component are measured to be  $\nu F_\nu (10^{15} \text{ Hz}) = (6 \pm 2)$  and  $(7 \pm 2) \times 10^{-13} \text{ erg cm}^{-2} \text{ s}^{-1}$ , respectively. These are comparable to the predicted synchrotron flux in the jet model of Toma et al. (2007);



see fig. 3 in Toma et al. (2007). The values calculated in Toma et al. (2007) for the UV/optical flux are  $\nu F_\nu(10^{15} \text{ Hz}) \approx 3$  and  $\approx 7 \times 10^{-13} \text{ erg cm}^{-2} \text{ s}^{-1}$  for 650 and 1250 s, respectively. Therefore, our observations of the UV/optical emission in the first 1350 s agree well with the jet model discussed in Toma et al. (2007) and this further strengthens the reasoning for a jet model to explain the observations from GRB 060218.

The presence of a jet, required to explain the UV/optical synchrotron emission, could induce some asphericity into the envelope. This reasoning for asphericity has been argued for both GRB/SN 1998bw (Maeda et al. 2002) and SN 2003jd (Mazzali et al. 2005). Aspherical expansion of the SN is favoured by Gorosabel et al. (2006), from the detection of linear polarization in SN 2006aj. Linear polarization in SNe has previously been linked with the non-spherical expansion of Type Ic SNe (Hoflich 1991). Furthermore, the detection of the linear polarization supports the jet model. Although we have shown that the observations do not disagree with a spherical model, a link between asphericity and SNe connected with GRBs has been seen in some studies (Mazzali et al. 2001; Maeda et al. 2002).

Conversely to a jet model to explain the observed emission from GRB 060218, Nakar (2015) argues that GRB 060218 and all other LLGRBs are produced from the shock breakout of a low-mass extended envelope that has choked the jet. Therefore, within their model, no emission from the jet or the interaction of the jet outside the extended envelope can be observed. However, this choked jet scenario is incompatible with our data, because it does not explain the synchrotron component seen in the UV/optical spectra before 1350 s. Also, the scenario does not address the blackbody component in the X-ray spectra at early times, before the breakout time-scale argued by Nakar (2015),  $t_{\text{BO}} \sim 1000$  s.

### 4.3 Host-galaxy reddening

Our best estimate of the host-galaxy reddening, an SMC extinction law and  $E(B - V) = 0.179 \pm 0.007$  mag, was obtained by assuming that the underlying UV/optical continuum has a Rayleigh-Jeans shape at all times between 5 and 60 ks after the GRB trigger. The reddening estimates used by Campana et al. (2006) and Waxman et al. (2007) were also based on the assumption of an underlying Rayleigh-Jeans shape, though with a less developed fitting procedure, and using the UV/optical SED from only one epoch (32 ks). They obtained  $E(B - V) = 0.20 \pm 0.03$  mag for an SMC extinction law, consistent with, but less precise than, the value we have obtained. The SMC extinction curve, which is favoured by our fits to GRB 060218, is usually found to be the best fit in GRB host galaxies (Schady et al. 2010). As with the majority of GRB host galaxies, the host galaxy of GRB 060218 also has a low metallicity, in this specific case  $12 + \log(\text{O}/\text{H}) \sim 0.07 Z_\odot$  (Wiersema et al. 2007).

Two alternative approaches to estimating the host-galaxy reddening towards GRB060218, which do not require any assumption about the underlying continuum shape, can be found in the literature: the equivalent width (EW) of the interstellar NaID (5895.9 Å) absorption line and the linear polarization. A measurement of the NaID absorption lines is reported in Guenther et al. (2006), and is translated to an estimate of  $E(B - V) = 0.04$  mag using the empirical relation between NaID EW and  $E(B - V)$  derived by Munari & Zwitter (1997) from observations of hot stars in the Milky Way. This reddening estimate is adopted in the works of Sollerman et al. (2006) and Pian et al. (2006). Munari & Zwitter (1997) suggest an uncertainty of 0.05 mag for  $E(B - V)$  derived in

this way, suggesting a host-galaxy reddening somewhat lower than our measurement, but it is not known whether the relation found by Munari & Zwitter (1997) is applicable for the lower metallicity, perhaps higher ionization ISM of the dwarf-galaxy host of GRB 060218. Gorosabel et al. (2006) observed a stable linear polarization of  $1.4 \pm 0.1$  per cent in SN 2006aj at 13 and 19 d after GRB 060218, and suggested that the host-galaxy ISM may be responsible for the polarization. Gorosabel et al. (2006) used this measurement together with the empirical relation obtained by Serkowski, Mathewson & Ford (1975) relating polarization to reddening in the Milky Way,  $P \leq 9E(B - V)$ . The implied host-galaxy reddening is  $E(B - V) \geq 0.15$  mag. This value is somewhat higher than the estimate based on NaID, and is consistent with our measurement of the host-galaxy reddening. However, we note a similar caveat as for the NaID measurement: it is not known to what degree the relation found by Serkowski et al. (1975) is applicable for the dust species in the lower metallicity ISM of the dwarf-galaxy host of GRB 060218. Given their inherent uncertainties, we consider that the NaID and polarization-based estimates of the host reddening are compatible with our measurement of  $E(B - V) = 0.179 \pm 0.007$  mag.

### 4.4 The blackbody emission component(s) and the geometry of the emission

We have shown that an outflowing blackbody component contributes to the SED at optical, UV, and X-ray energies. The outflowing blackbody emission peaking at X-ray energies before 10 ks and the Rayleigh-Jeans spectral shape in the UV/optical at coinciding times support the notion that we are observing the same blackbody component in both energy ranges. In contrast, to explain the thermal emission observed in the X-ray and UV/optical, Waxman et al. (2007) require that the thermal component in the UV/optical arises from a separate region to that of the thermal component in the X-ray. In their model, the thermal X-ray emission is produced from a compressed wind shell, while the thermal UV/optical emission is produced at a lower temperature in the outer shells of the progenitor star. Thus, in the model of Waxman et al. (2007) the X-ray emission originates further from the progenitor star than the UV/optical emission. However, for a blackbody of lower temperature to dominate the emission of a higher temperature blackbody, it must have a larger surface area, and therefore one would expect it to arise at a greater, rather than smaller radius around the progenitor star. We cannot envisage a geometrical configuration in which a region of lower temperature, and at a significantly smaller distance from the progenitor star, than that giving rise to the blackbody emission observed in the X-ray could produce emission that would dominate in the UV/optical. Therefore, we consider our spectral model, in which the UV/optical and thermal X-ray emission are produced by the same blackbody component, to be more compelling than the two-component description advocated by Waxman et al. (2007).

Ghisellini et al. (2007b) investigated the possibility that the UV/optical and X-ray radiation belonged to a single blackbody. They used the photospheric radius model in Waxman et al. (2007) to get a temporal relation for the radius.

$$R = R_0 + 3.6 \times 10^{10} (t - t_0)^{0.80} \text{ cm.} \quad (6)$$

They assumed that the UV/optical emission before 120 ks corresponds to the Rayleigh-Jeans part of the blackbody spectrum and used the observed UV/optical fluxes to determine the blackbody luminosity. They then estimated the associated energy emitted by the blackbody at each step of their UV/optical light curve using  $L \Delta t$ ,

where  $\Delta t$  was the time period for the UV/optical flux measurement. Ghisellini et al. (2007b) argued that the energy emitted by the blackbody was too large ( $E_{\text{BB}} \sim 10^{51}$  erg) to be viable when compared to the total kinetic energy of the SN explosion,  $E_{\text{SN,K}} \sim 2 \times 10^{51}$  erg (Mazzali et al. 2006).

We find that the blackbody energy is smaller at early times ( $< 1350$  s) than Ghisellini et al. (2007b), because we have found that the UV/optical emission is dominated by a synchrotron component at these times. We have made our own estimate of the energy emitted by the blackbody by integrating the luminosity of the blackbody model component with respect to time. We find that during the initial 650–2700 s the integrated luminosity of the blackbody is  $E = 1.1 \times 10^{51}$  erg. Thus, our spectral modelling leads to a similar energetic requirement to that raised by Ghisellini et al. (2007b). The large amount of energy radiated by the blackbody would suggest a more energetic SN than that inferred by Mazzali et al. (2006), for example  $E_{\text{SN,K}} = 10^{52}$  erg as found by Cano (2013), which is more consistent with the SNe usually associated with GRBs.

From equation (5), we can see that our calculated breakout radius,  $R_0 = 2.3 \times 10^{13}$  cm, far exceeds the typical radius of a WR star ( $\sim 10^{11}$  cm), which is the preferred candidate for the progenitor (Campana et al. 2006). Waxman et al. (2007) propose two possibilities for explaining the large breakout radius. The first is that the star is surrounded by an optically thick shell, formed by a large mass-loss event from the progenitor star that occurred before the SN explosion. The second is that a dense stellar wind can be optically thick to a large radius. Nakar & Piro (2014) advocate the former, whereas Li (2007) discusses the latter. Our value for  $R_0$  exceeds considerably even the breakout radius of  $7.8 \times 10^{12}$  cm derived by Waxman et al. (2007), in their model of a wind from a WR star. A progenitor star that is larger than a WR star (e.g.  $100 R_{\odot}$ ) with a WR-like wind (Li 2007), or a significant pre-explosion mass-loss event, could account for the  $R_0$  that we derive.

From our observations, we calculated the velocities from the spherical outflow model using the derivative of the blackbody radius against time. The inferred velocities from the spherically outflowing blackbody range from  $65\,400 \text{ km s}^{-1}$  at 1615 s to  $16\,800 \text{ km s}^{-1}$  at 120 ks. Extrapolating equation (5) to 2.89 d gives a velocity of  $v = (15\,000 \pm 4000) \text{ km s}^{-1}$ , which is inconsistent with the velocity calculated in Pian et al. (2006) from the spectroscopic analysis of SN 2006aj at 2.89 d,  $v = 26\,000 \text{ km s}^{-1}$ . However, if we fit a power-law plus constant model to the velocity data for GRB 060218 from Pian et al. (2006), we find  $v \propto t^{-0.3}$  and this is in good agreement with our prediction for the velocity of  $v \propto t^{-0.32 \pm 0.01}$ . Our inconsistency with the velocity measurement by Pian et al. (2006) at 2.89 d could be because the velocities calculated in Pian et al. (2006) are measured from the Doppler shift in the absorption lines from the velocity in the line of sight to the observer. Our velocities are measured in the transverse direction. A non-spherical expansion that is faster in the line-of-sight direction would produce such a discrepancy between the line of sight and transverse velocities, and hence could account for the difference between the velocities we have derived and those derived by Pian et al. (2006).

## 5 CONCLUSIONS

The work in this paper analyses the early UV/optical emission and the thermal components observed in both the UV/optical and X-ray, in GRB 060218.

We have shown that the observed UV/optical spectral index at early times indicates that before thermal emission dominates the

UV/optical, the UV/optical emission is the GRB afterglow. We have proposed that the UV/optical afterglow is likely to be produced from external shock synchrotron emission from a jet; additionally, the same mechanism can be used to explain the radio emission at later times ( $\gtrsim 2$  d), as explained by Toma et al. (2007). Conversely, after the initial observations of the UV/optical synchrotron component, the UV/optical spectrum resembles a Rayleigh-Jeans spectral shape  $F_{\nu} \propto \nu^2$  at  $t > 1350$  s, until the blackbody peak is measured in the UV/optical bands at 120 ks.

We have proposed a basic model that accounts for most of the observed features in GRB 060218. This model includes a jet that penetrates the envelope surrounding the progenitor core. The extended envelope is optically thick and emits UV/optical and thermal X-ray emission from the same expanding region. Within the time interval of 1400–8000 s, the UV/optical emission corresponds to the same blackbody spectrum as the X-ray emission. The photosphere continues to expand, and at 120 ks, the thermal UV/optical emission is observed when the blackbody is peaking at UV energies. Our basic model improves upon previous models, because we have shown the evidence for a jet that is needed to produce the UV/optical emission during  $t \leq 1350$  s and this UV/optical jet signature has not been recognized in previous studies of GRB 060218. The synchrotron component observed in the UV/optical agrees with the late observations of a synchrotron component in the radio emission. Furthermore, we have shown that the UV/optical and X-ray blackbody emission can be produced in the same region and can be produced in a spherical outflow.

We have demonstrated that the UV/optical emission during 5–60 ks could be characterized by Rayleigh-Jeans emission. We have shown that the UV/optical spectral shape does not change during this time, and this provided us with an accurate value of the UV/optical reddening, and moreover allowed us to rule out a Milky Way extinction curve for the host galaxy.

Finally, it is important to note that GRB 060218 is one of only four LLGRBs observed, providing a rare opportunity to analyse the early UV/optical emission in the very early stages of an SN. If our interpretation is correct, GRB 060218 represents the first LLGRB with a clear observed UV/optical afterglow, which is valuable in understanding what is happening to produce this emission. It is proposed that this is the product of a jet penetrating the progenitor envelope and interacting with the surrounding medium. Our proposed model has implications on future observations of LLGRBs and also highlights the importance of UV/optical observations during the prompt emission of LLGRBs, as this is the only time where the observation of the UV/optical afterglow is possible before the dominant emission from a thermal photospheric component.

## ACKNOWLEDGEMENTS

We thank D. González Caniulef for helpful discussions. SWKE acknowledges support from the Science and Technology Facilities Council (STFC; grant number ST/N504488/1). MJP acknowledges support from STFC (grant number ST/N000811/1). MJP, AAB, and NPMK acknowledge support from the United Kingdom Space Agency (UKSA; grant number ST/P002323/1). This research has made use of data from the High Energy Astrophysics Science Archive Research Center (HEASARC) and the UK Swift Science Data Centre, provided by NASA's Goddard Space Flight Center and the Department of Physics and Astronomy, Leicester University, UK, respectively.

## REFERENCES

- Abbott B. P. et al., 2017, *ApJ*, 848, 12
- Amati L. et al., 2002, *A&A*, 390, 81
- Band D. et al., 1993, *ApJ*, 413, 281
- Barthelmy S. D. et al., 2005, *Space Sci. Rev.*, 120, 143
- Breeveld A. A. et al., 2010, *MNRAS*, 406, 1687
- Breeveld A. A., Landsman W., Holland S. T., Roming P., Kuin N. P. M., Page M. J., 2011, *AIP Conf. Proc. Vol. 1358, Gamma Ray Bursts 2010*. Am. Inst. Phys., New York, p. 373
- Burrows D. N. et al., 2005, *Space Sci. Rev.*, 120, 165
- Campana S. et al., 2006, *Nature*, 442, 1008
- Cano Z., 2013, *MNRAS*, 434, 1098
- Cano Z., Wang S. Q., Dai Z. G., Wu X. F., 2017, *Adv. Astron.*, 2017, 8929054, Available at: <http://adsabs.harvard.edu/abs/2017AdAst2017E...5C>
- Capaldi M., Perri M., Saija B., Tamburelli F., Angelini L., 2005, The Swift XRT Data Reduction Guide, Version 1.2. Available at: <http://heasarc.nasa.gov/docs/swift/analysis/>
- Cusumano G., Barthelmy S., Gehrels N., Hunsberger S., Immler S., Marshall F., Palmer D., Sakamoto T., 2006, GCN Circ. (GRB Coordinates Network), 4775, 1, Available at: <http://adsabs.harvard.edu/abs/2006GCN..4775....1C>
- Fan Y.-Z., Piran T., Xu D., 2006, *J. Cosmol. Astropart. Phys.*, 09, 013
- Galama T. J. et al., 1998, *Nature*, 395, 670
- Gehrels et al., 2004, *ApJ*, 611, 1005
- Ghisellini G., Ghirlanda G., Tavecchio F., 2007a, *MNRAS*, 375, L36
- Ghisellini G., Ghirlanda G., Tavecchio F., 2007b, *MNRAS*, 382, L77
- Gorosabel J. et al., 2006, *A&A*, 459, L33
- Guenther E. W., Klose S., Vreeswijk P., Pian E., Greiner J., 2006, GCN Circ. (GRB Coordinates Network), 4863, 1. Available at: <http://adsabs.harvard.edu/abs/2006GCN..4863....1G>
- Guiriec S. et al., 2011, *ApJ*, 727, L33
- Guiriec S. et al., 2016, *ApJ*, 831, L8
- Hoflich P., 1991, *A&A*, 246, 481
- Irwin C. M., Chevalier R. A., 2016, *MNRAS*, 460, 1680
- Kalberla P. M. W., Burton W. B., Hartmann D., Arnal E. M., Bajaja E., Morras R., Pöppel W. G. L., 2005, *A&A*, 440, 775
- Kann D. A. et al., 2010, *ApJ*, 720, 1513
- Kouveliotou C., Meegan C. A., Fishman G. J., Bhat N. P., Briggs M. S., Koshut T. M., Paciesas W. S., Pendleton G. N., 1993, *ApJ*, 413, L101
- Liang E.-W., Zhang B.-B., Stamatikos M., Zhang B., Norris J., Gehrels N., Zhang J., Dai Z. G., 2006, *ApJ*, 653, L81
- Li L.-X., 2007, *MNRAS*, 375, 240
- MacFadyen A. I., Woosley S. E., 1999, *ApJ*, 524, 262
- Maeda K., Nakamura T., Nomoto K., Mazzali P. A., Patat F., Hachisu I., 2002, *ApJ*, 565, 405
- Mazzali P. A. et al., 2005, *Science*, 308, 1284
- Mazzali P. A. et al., 2006, *Nature*, 442, 1018
- Mazzali P. A., Nomoto K., Patat F., Maeda K., 2001, *ApJ*, 559, 1047
- Mészáros P., Rees M. J., 1997, *ApJ*, 476, 232
- Michałowski M. J. et al., 2018, *A&A*, 616, A169
- Millard J. et al., 1999, *ApJ*, 527, 746
- Munari U., Zwitter T., 1997, *A&A*, 318, 269
- Nakar E., 2015, *ApJ*, 807, 172
- Nakar E., Piro A. L., 2014, *ApJ*, 788, 193
- Norris J. P., Marani G. F., Bonnell J. T., 2000, *ApJ*, 534, 248
- Pian E. et al., 2006, *Nature*, 442, 1011
- Planck Collaboration I, 2016, *A&A*, 594, 13
- Poole T. S. et al., 2008, *MNRAS*, 383, 627
- Roming P. W. A. et al., 2005, *Space Sci. Rev.*, 120, 95
- Sari R., Piran T., Narayan R., 1998, *ApJ*, 497, L17
- Sazonov S. Y., Lutovinov A. A., Sunyaev R. A., 2004, *Nature*, 430, 646
- Schady P. et al., 2010, *MNRAS*, 401, 2773
- Schady P. et al., 2012, *A&A*, 537, A15
- Schlegel D. J., Finkbeiner D. P., Davis M., 1998, *ApJ*, 500, 525
- Serkowski K., Mathewson D. S., Ford V. L., 1975, *ApJ*, 196, 261
- Soderberg A. M. et al., 2006, *Nature*, 442, 1014
- Sollerman J. et al., 2006, *A&A*, 454, 503
- Toma K., Ioka K., Sakamoto T., Nakamura T., 2007, *ApJ*, 659, 1420
- Ukwatta T. N. et al., 2012, *MNRAS*, 419, 614
- Virgili F. J. et al., 2013, *ApJ*, 778, 54
- Waxman E., Mészáros P., Campana S., 2007, *ApJ*, 667, 351
- Wiersema K. et al., 2007, *A&A*, 464, 529
- Woosley S. E., 1993a, *ApJ*, 405, 273
- Woosley S. E., Heger A., Weaver T. A., 2002, *Rev. Mod. Phys.*, 74, 1015

## APPENDIX A: SED FIGURES

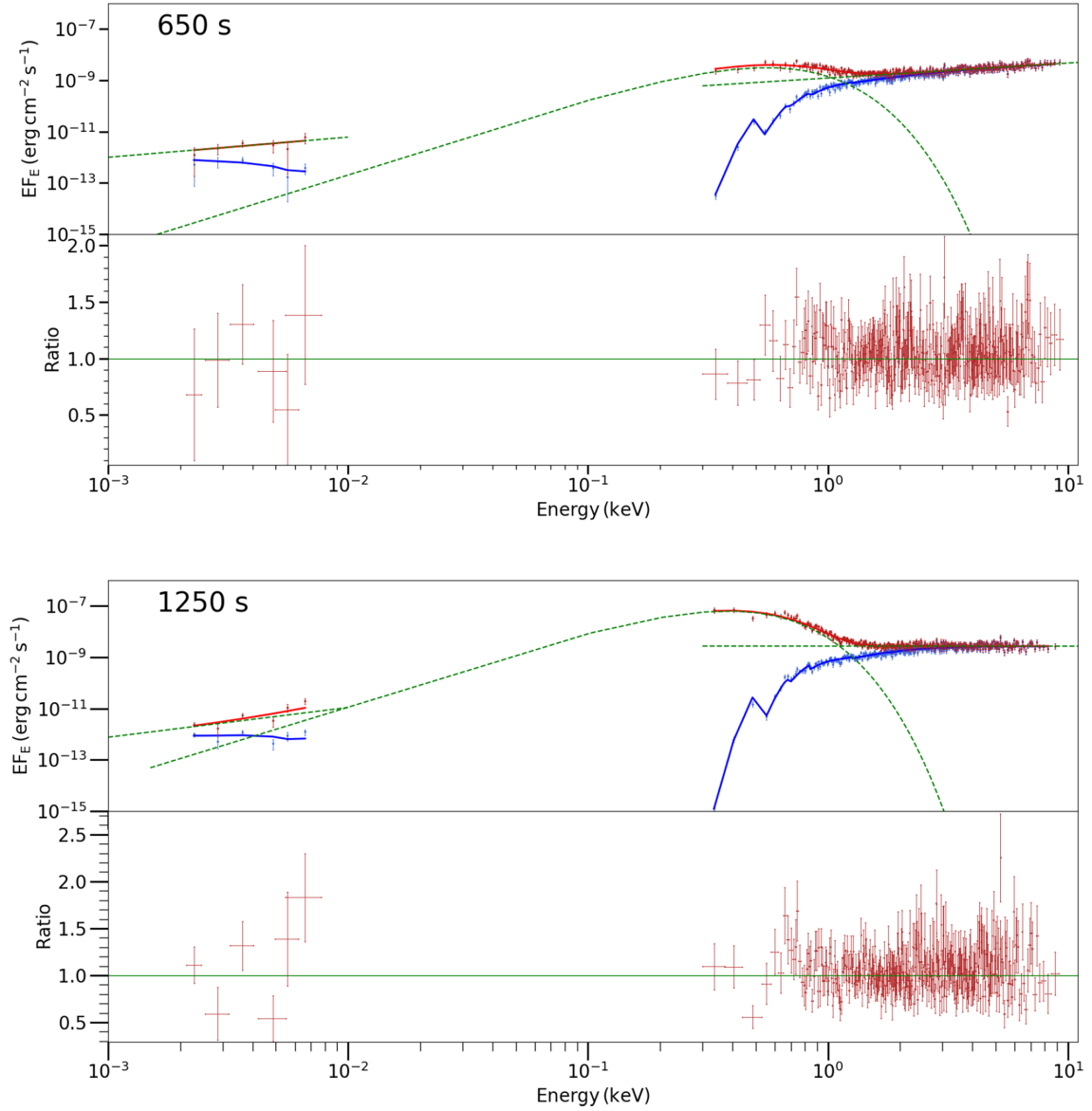


**Figure A1.** The SEDs of GRB 060218 for all of the times shown in Table 1. The SEDs are shown across the UV/optical and X-ray energies (0.0015–10 keV). The models used in the fitting are listed in Table 2. We display the flux as  $EF_E$ . The red data points represent the dereddened UV/optical and unabsorbed X-ray flux. The blue data points represent the UV/optical and X-ray flux including absorption as measured by UVOT and XRT. The dashed lines represent the model components. The bottom panel of the figure shows the ratio of the data to overall model.



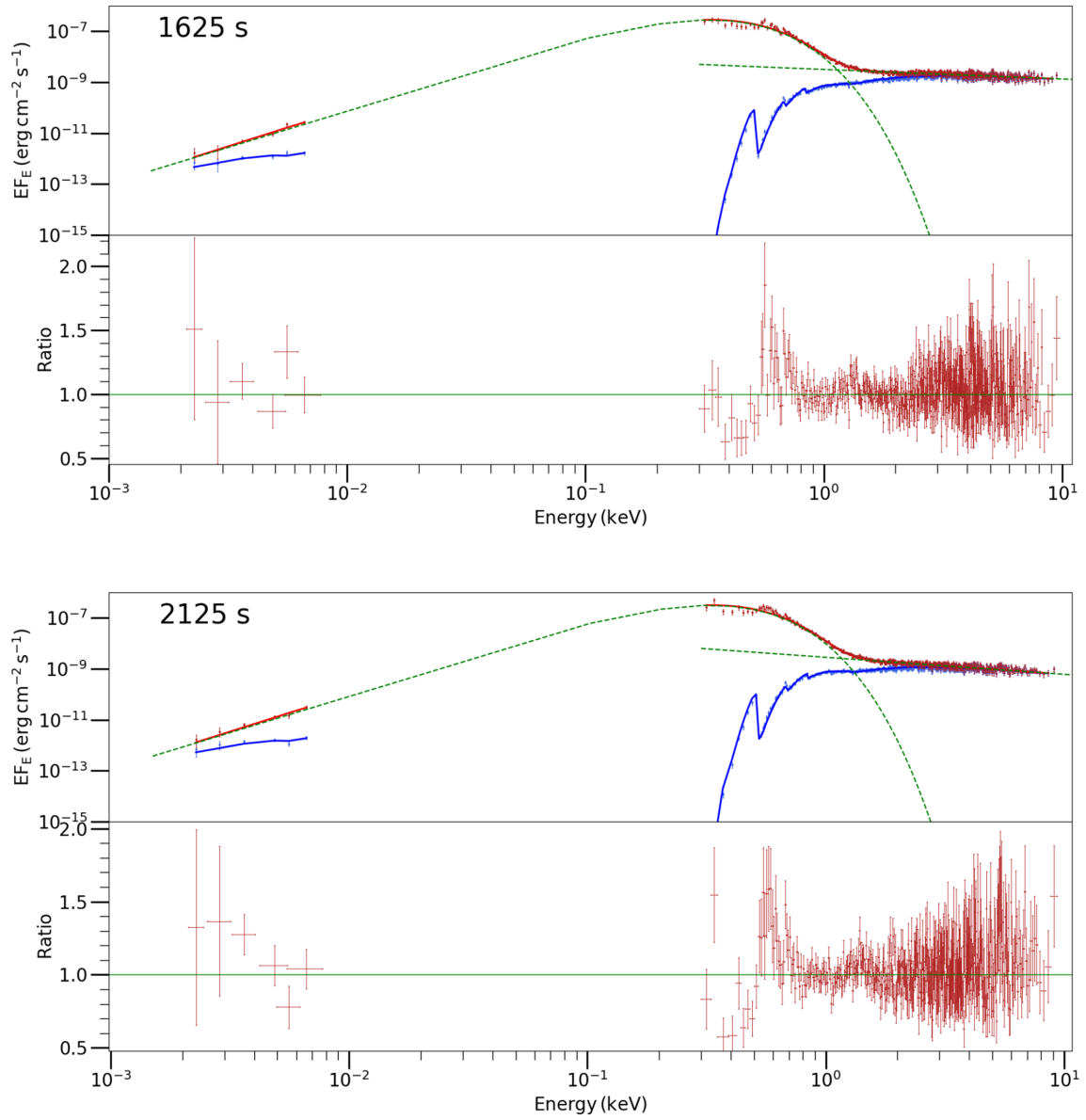


Figure A1 – continued

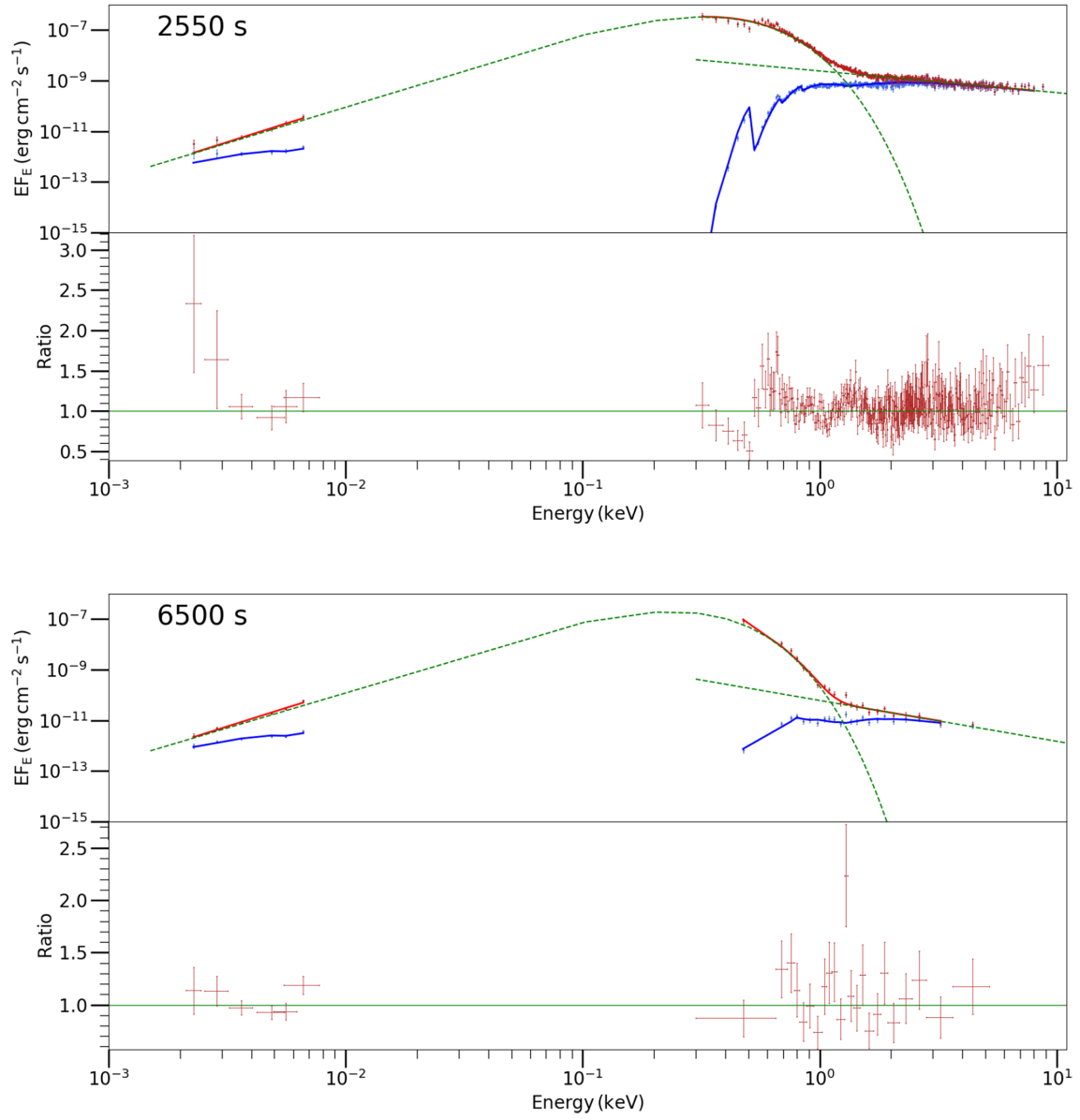
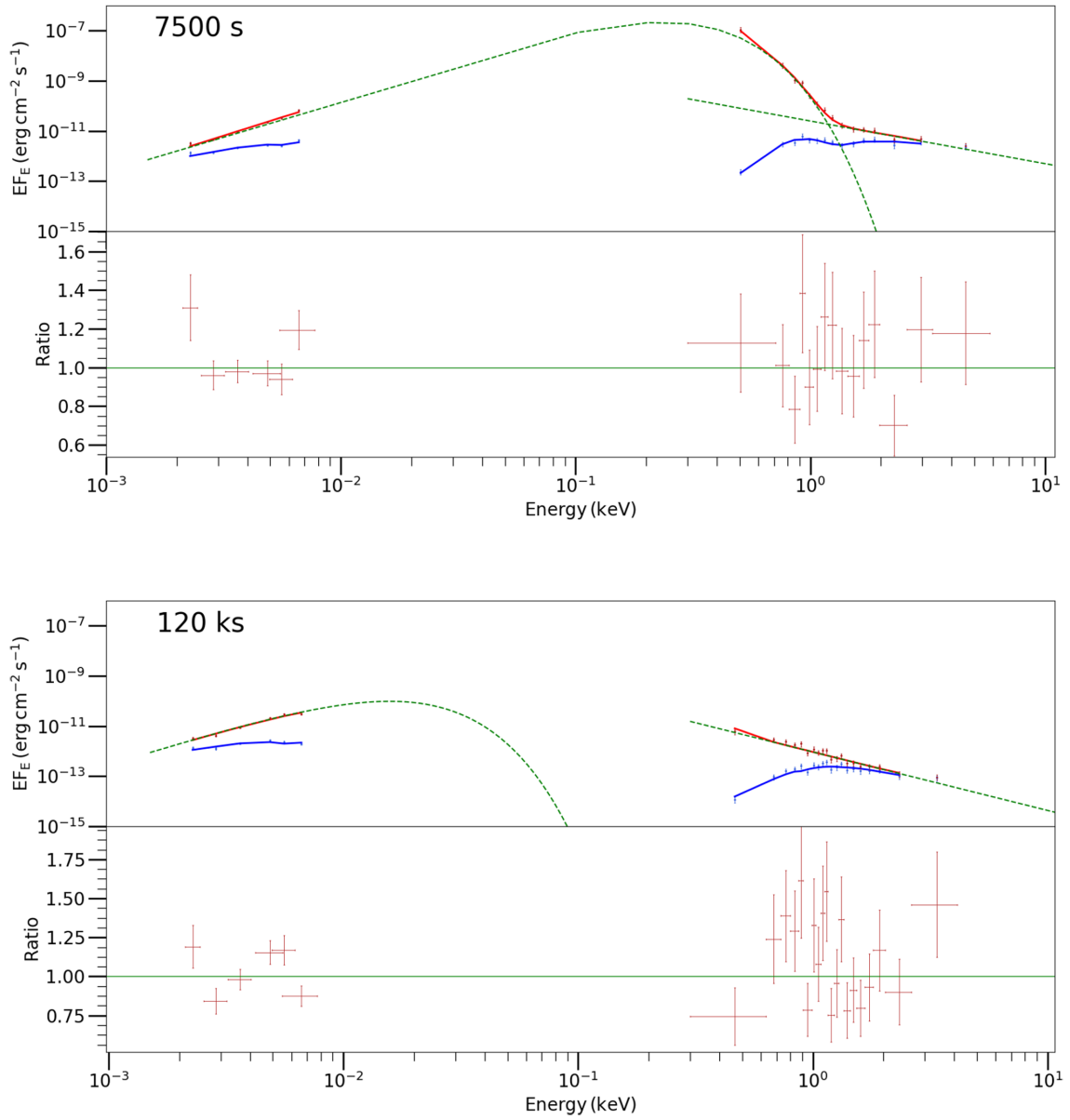


Figure A1 – continued

**Figure A1** – *continued*

This paper has been typeset from a  $\text{\LaTeX}$  file prepared by the author.